

Design Rules for Laser-Treated Icephobic Metallic Surfaces for Aeronautic Applications

Vittorio Vercillo,* Simone Tonnichia, Jean-Michel Romano, Antonio García-Girón, Alfredo I. Aguilar-Morales, Sabri Alamri, Stefan S. Dimov, Tim Kunze, Andrés Fabián Lasagni, and Elmar Bonaccorso*

Ice accretion on external aircraft surfaces due to the impact of supercooled water droplets can negatively affect the aerodynamic performance and reduce the operational capability and, therefore, must be prevented. Icephobic coatings capable of reducing the adhesion strength of ice to a surface represent a promising technology to support thermal or mechanical ice protection systems. Icephobicity is similar to hydrophobicity in several aspects and superhydrophobic surfaces embody a straightforward solution to the ice adhesion problem. Short/ultrashort pulsed laser surface treatments are proposed as a viable technology to generate superhydrophobic properties on metallic surfaces. However, it has not yet been verified whether such surfaces are generally icephobic under representative icing conditions. This study investigates the ice adhesion strength on Ti6Al4V, an alloy commonly used for aerospace components, textured by means of direct laser writing, direct laser interference patterning, and laser-induced periodic surface structures laser sources with pulse durations ranging from nano- to femtosecond regimes. A clear relation between the spatial period, the surface microstructure depth, and the ice adhesion strength under different icing conditions is investigated. From these observations, a set of design rules can be defined for superhydrophobic surfaces that are icephobic, too.

can reduce dramatically lift and increase drag, influencing the maneuverability of the aircraft. Ice protection systems (IPS) are installed to allow aircraft flying safely in icing conditions. At the present time, IPS are not supported by coatings or surfaces that facilitate the ice removal—due to the still too low maturity and robustness of such technological solutions. Yet, surface functionalization is a promising strategy for manufacturing icephobic surfaces^[3] aiming to delay ice accretion and/or to reduce ice adhesion^[4,5] and therefore to reduce the electrical or thermal energy required by the IPS.

In the last two decades, several approaches for producing icephobic surfaces were presented in literature. For example, it has been proven that polishing the surfaces can reduce the mechanical interlocking with the accreted ice, hence facilitating the ice removal.^[5] Coatings can lower the surface free energy and thus reduce the strength of the bonding between ice and surface.^[6] On slippery liquid-infused porous surfaces the super-


cooled water droplets impinge on a liquid instead of a solid surface, which offers a double advantage: interfacial slippage of water or ice occurs (nonzero slip velocity)—which reduces ice adhesion^[7]—and interlocking of ice with a liquid interface cannot occur. However, employing coatings or chemicals to

1. Introduction

Icing is a topic of major concern in the aviation industry, since ice accretion affects and restricts flight operations of aircraft.^[1,2] Even small ice formations on the leading edge of the wings

V. Vercillo, S. Tonnichia, Dr. E. Bonaccorso
Airbus Central Research and Technology, Materials X
Willy-Messerschmitt-Str. 1, 82024 Taufkirchen, Germany
E-mail: vittorio.vercillo@airbus.com; elmar.bonaccorso@airbus.com

V. Vercillo, Prof. A. F. Lasagni
Institut für Fertigungstechnik
Technische Universität Dresden
George-Bähr-Str. 3c, 01069 Dresden, Germany

 The ORCID identification number(s) for the author(s) of this article can be found under <https://doi.org/10.1002/adfm.201910268>.

© 2020 The Authors. Published by WILEY-VCH Verlag GmbH & Co. KGaA, Weinheim. This is an open access article under the terms of the Creative Commons Attribution License, which permits use, distribution and reproduction in any medium, provided the original work is properly cited.

DOI: 10.1002/adfm.201910268

S. Tonnichia
Department of Chemical Engineering
Materials, Environment
INSTM Laboratory for Engineering of Surface Treatments
Sapienza University of Rome
via Eudossiana 18, 00184 Rome, Italy

Dr. J.-M. Romano, A. García-Girón, Prof. S. S. Dimov
School of Engineering
University of Birmingham
Edgbaston, Birmingham B15 2TT, UK

A. I. Aguilar-Morales, S. Alamri, Dr. T. Kunze, Prof. A. F. Lasagni
Fraunhofer-Institut für Werkstoff- und Strahltechnik IWS
Winterbergstr. 28, 01277 Dresden, Germany

treat the surface presents several difficulties. First, large areas must be coated homogeneously. Additionally, the use of chemicals and the creation of toxic byproducts have an impact both for the environment and for the operators applying those paints.^[8] Another approach consists in manufacturing superhydrophobic surfaces that mimic, for instance, the lotus-leaf effect.^[9–11] In this natural example, water droplets rest on top of micro- and nanostructures in a Cassie–Baxter nonwetting state,^[12] instead of wetting entirely the surface and spreading out into a thin water film. Due to the strong water repellent properties,^[9] superhydrophobic surfaces are considered a promising solution to obtain icephobic surfaces, too, and to tackle the ice adhesion problem.^[13–15] Different mechanisms have been proposed to explain how superhydrophobicity can be linked to icephobicity. For example, superhydrophobic surfaces could minimize the contact time during water droplet impact,^[16] delay heterogeneous nucleation of supercooled water,^[17–19] or promote the shedding of water droplets before they can freeze.^[13,20] Superhydrophobic micro/nanostructured surfaces were also implemented on airfoils and tested under icing conditions.^[21] Antonini et al. showed that the combination of a superhydrophobic coating with an active IPS produces a significant reduction of heating power (up to 80% heating power saving) needed to keep the leading edge of the sample free of ice. Additionally, a reduction or prevention of runback ice, depending on the test condition, was observed, likely due to the shedding of the droplets before freezing.^[14] De Pawn and Dolatabadi followed a similar approach and showed that a superhydrophobic surface can effectively reduce ice accretion and prevent runback ice with respect to an untreated aluminum airfoil surface.^[22] Finally, in literature it is still debated whether dual scale hierarchical micro/nanostructured superhydrophobic surfaces or single scale nanostructured superhydrophobic surfaces embody a more effective solution to tackle icing phenomena. Shen et al. found that a single scale nanostructured superhydrophobic surface accumulates less ice than a hierarchical micro/nanostructured superhydrophobic surface, suggesting that the latter typology could experience a penetration of the μm -sized droplets into the microstructures.^[23] On the other hand, Milles et al. showed that a impacting water droplet has a higher mobility on cold dual scale hierarchical superhydrophobic surface, producing an increased freezing delay than a single scale superhydrophobic surface.^[19]

Among the several approaches that can be used to generate lotus leaf-like structures on surfaces,^[24–26] short/ultrashort (S/US) laser pulses present several advantages. The material removal takes place locally at the zone where the laser beam is interacting with the substrate and also causes a limited chemical surface modification.^[27] From an industrial point of view, S/US pulsed laser technologies are very flexible and allow to treat a wide range of materials as long as the substrate absorbs the used laser wavelength (i.e., infrared (IR) and visible (VIS) for metals^[28,29] and ultraviolet (UV) for polymers^[30]). In addition, the scale-up of such technologies for industrial applications has been already demonstrated in several cases.^[31–34]

Nevertheless, the surface laser treatment can have a detrimental effect on the mechanical properties of the final component, in particular in terms of fatigue resistance. However, in this work it is envisioned to manufacture such surface modifications on the nonstructural metallic foils covering the leading

edge of the wings and winglets, which are not required to withstand high mechanical loads.

Different laser processes and pulse durations have been used to tune the surface wettability of metals by generating hierarchically structured superhydrophobic surfaces.^[35–38] Many of these works suggest that such surfaces can be also used for icephobic applications.^[39–41] In a research previously published, it was shown that Ti6Al4V (Ti64) offers a robust substrate for the laser-generated features compared to Aluminum Alloy 2024 (AA2024), since these features providing the support for the Cassie–Baxter state remain unchanged on Ti64 after 16 icing/deicing cycles, while are partially destroyed on the AA2024. Additionally, the Ti64 surface chemically functionalized with a perfluoropolyether solution in a fluorinated solvent (MecaSurf, Surfactis Technologies, Angers, France) is still superhydrophobic after 16 icing/deicing cycles, while the nonfunctionalized laser-treated Ti64 increases its wettability (static contact angle (CA) decreases from $\approx 170^\circ$ to 120°) due to the removal of an adsorbed C-rich layer on its surface.^[42] However, to the best of our knowledge it has not yet been addressed which kind of microstructure (and therefore which laser technology) can produce superhydrophobic surfaces that also show icephobic properties in atmospheric icing conditions encountered during aircraft operations. To bridge this gap, this work investigates the adhesion strength of impact ice (i.e., ice generated in close to operation conditions in icing wind tunnel tests) on laser-structured Ti64 superhydrophobic surfaces patterned employing three different laser techniques: direct laser writing (DLW), direct laser interference patterning (DLIP), and laser induced periodic surface structures (LIPSS), with pulse durations in the range of nanosecond to femtoseconds.

During the DLW and LIPSS processes, the laser beam is focused on the surface of the sample and the scanning of the beam textures a defined area.^[43] LIPSS are self-organized surface features usually generated with fluences close to or slightly above the ablation threshold.^[44] By optimizing the energy transferred to the surface, sub-micrometer features or hierarchical micro/nanoscale features can be fabricated.^[45] On the other hand, DLIP relies its principle on the overlap of multiple coherent laser beams to generate defined interference patterns within the laser beam profile and to produce features in the micro- and sub-micrometer scale.^[46] The method has been successfully applied for treating materials such as metals, polymers, or organic coatings^[47,48] with process rates up to $0.9 \text{ m}^2 \text{ min}^{-1}$.^[31] A systematic analysis of the results allowed us to propose design rules for surface features that most effectively reduce the ice adhesion strength of impact ice on metallic surfaces.

2. Results and Discussion

2.1. Surface Manufacturing and Characterization

Using DLIP, DLW, and LIPSS fabrication techniques, a diverse range of Ti64 substrates were processed. **Figure 1a–j** shows scanning electron microscopy (SEM) images of representative surface topographies investigated in this research. The used laser processing parameters are listed in Table S1 in the Supporting Information and additional SEM images of surface topographies can also be found in Figure S1a–h in the Supporting Information.

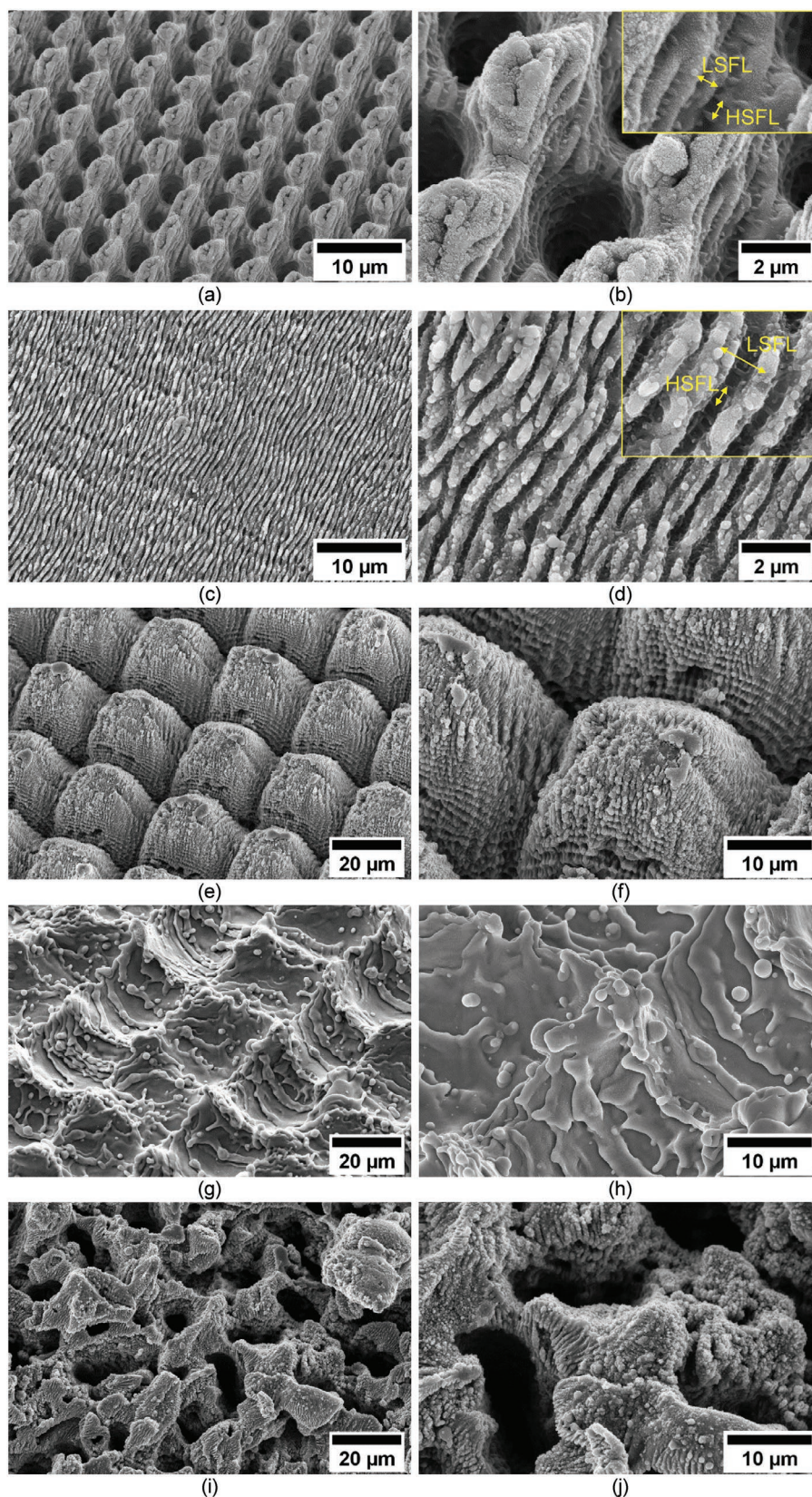


Figure 1. SEM images of a,b) DLIP 2 surface (the arrows describe the periodicities of LSFL and HSFL), c,d) LIPSS 2 surface (the arrows describe the periodicities of LSFL and HSFL), e,f) LOTUS 2 topography, g,h) ROUGH 2 surface, and i,j) POROUS surface.

Two different microstructures were fabricated using DLIP, i.e., with spatial periods Λ (pillar-to-pillar distance) of $\approx 2.7 \mu\text{m}$ (DLIP 1) and $\approx 5.4 \mu\text{m}$ (DLIP 2, Figure 1a,b), respectively. Both surfaces have pillars with an average depth at the maxima–maxima positions of 1.8 ± 0.25 and $3.0 \pm 0.23 \mu\text{m}$, correspondingly. As reported for Ti64 surfaces treated with ps-DLIP,^[38] the laser-treated samples show additional surface features, which can be identified as low spatial frequency LIPSS (LSFL) with a spatial period of $\approx 400 \text{ nm}$. High spatial frequency LIPSS (HSFL) can be observed in perpendicular direction to the LSFL (inset in Figure 1b).^[44] In the last case, the measured lateral size of the HSFL was 200 nm. Thus, both DLIP samples consist of hierarchical micro/nano-structured surfaces.

The samples LIPSS 1 and LIPSS 2 (Figure 1c,d) are characterized by sub-micrometric single-scale structures, fabricated using DLW. Both surfaces have ripples (LSFL) with a spatial period Λ of $\approx 700 \text{ nm}$ for LIPSS 1 and $\approx 800 \text{ nm}$ for LIPSS 2. HSFL are perpendicular to the LSFL with a spatial period of 150 nm (inset in Figure 1d). Furthermore, two lotus-like surfaces were produced using fs-DLW: both topographies (LOTUS 1 and 2, see for instance Figure 1e,f) present a hierarchical micro/nanostructured surface consisting of micrometric pillars covered uniformly by nanometric LIPSS (LSFL). The LOTUS 1 and 2 surfaces have, respectively, a spatial period Λ of ≈ 27 and $25 \mu\text{m}$ and a depth of ≈ 8 and $13 \mu\text{m}$. The spatial period of the LSFL is $\approx 650 \text{ nm}$ on the LOTUS 1 and 450 nm on the LOTUS 2.

A ns-DLW process was used to fabricate a periodic roughness on two surfaces, called Roughness 1 (ROUGH 1) and Roughness 2 (ROUGH 2, Figure 1g,h). In this case, the resulting structures have features only in the micrometer range, with very few recast solidified nanobubbles.^[49] The spatial period Λ on both ROUGH 1 and 2 surfaces is $\approx 26 \mu\text{m}$ while their depths are ≈ 14 and $20 \mu\text{m}$, respectively. The thermal effects induced by the laser in the material are not negligible in this case (due to the long pulse duration) and the microstructures are composed from molten and resolidified material.

Table 1. Laser patterns produced on the surfaces with relevant surface properties: static contact angle (CA) and roll-off angle (RoA), average (R_s), and peak-to-peak (R_z) roughness.

Sample	Water contact angle, CA [°]	Water roll-off angle, RoA [°]	Average roughness, R_s [μm]	Peak-to-peak roughness, R_z [μm]	Period, Λ [μm]
Reference	51 ± 2	>90	0.50 ± 0.03	3.97 ± 0.17	–
DLIP 1	163 ± 6	8 ± 6	0.47 ± 0.03	3.95 ± 0.29	2.7
DLIP 2	163 ± 2	11 ± 3	0.60 ± 0.04	4.54 ± 0.49	5.4
LIPSS 1	169 ± 3	9 ± 4	0.45 ± 0.01	3.41 ± 0.21	0.7
LIPSS 2	163 ± 3	8 ± 7	0.47 ± 0.01	3.75 ± 0.28	0.8
LOTUS 1	167 ± 2	9 ± 5	1.39 ± 0.07	8.37 ± 0.49	25
LOTUS 2	168 ± 2	4 ± 3	2.65 ± 0.01	12.46 ± 0.08	27
ROUGH 1	168 ± 2	2 ± 2	2.42 ± 0.05	14.40 ± 0.08	26
ROUGH 2	169 ± 2	4 ± 3	3.28 ± 0.06	19.46 ± 0.25	25
POROUS	168 ± 2	2 ± 2	4.24 ± 0.18	26.53 ± 1.32	20+40

Finally, a fs-DLW process was used to produce randomly oriented surface structures. An example of fabricated porous structure is shown in Figure 1(i,j) (called POROUS). The images show that in this case also a hierarchical micro/nanostructured surface was generated, since the randomly oriented microstructures are covered with LIPSS (LSFL, spatial period $\Lambda \approx 500$ nm). SEM images of the structured samples denoted as DLIP 1, LIPSS 1, LOTUS 1, and ROUGH 1 can be found in Figure S1a–h in the Supporting Information.

Table 1 describes the surface roughness and the wettability properties of all surfaces. After the laser texturing, the samples were treated with a hydrophobizing agent and the water CA have been measured. As a result, all combinations of laser parameters used yielded superhydrophobic properties on all Ti64 samples, showing CA higher than 150° while roll-of-angles (RoA) lower than 15°, which are typical values for a Cassie–Baxter wetting state.^[12]

In spite of the excellent results in terms of hydrophobicity, the wettability assessment has been performed in conditions very different from the ones encountered during in-flight icing. In particular, the water droplets are at room temperature, have diameters of the order of few millimeters—i.e., similar to the capillary length of water which is ≈ 2.7 mm—and are carefully deposited on the surfaces. On the contrary, in an icing encounter, the droplets are supercooled, have diameters of the order of tens of micrometers—i.e., much smaller than the capillary length of water—and impact the surface at speeds higher than 50 m s⁻¹. Therefore, one of the aims of our investigation is to assess whether superhydrophobic surfaces also show icephobic properties in in-flight icing conditions and to identify which kind of microstructures perform better under these conditions.

2.2. Ice Adhesion Testing

In order to understand if superhydrophobicity assessed in standard lab conditions can be linked to icephobicity, ice adhesion tests were performed in an icing wind tunnel iCORE (icing and CONTamination REsearch facility^[50]). The iCORE can simulate atmospheric in-flight icing conditions generating a cloud of representative supercooled water droplets with a median volume diameter (MVD) of ≈ 20 μm.^[51]

Four different icing conditions were used, corresponding to four representative atmospheric ice types and achieved by distinct freezing fractions (FF). The FF parameter includes all the information related to the atmospheric parameters such as true air speed (TAS), total air temperature (TAT), liquid water content (LWC) and MVD, hence to the icing conditions.^[52,53] The FF can be used to simplify the description of ice types, since it represents the amount of supercooled water that freezes upon impact. If the water does not freeze at all FF = 0. Rime forms when all impinging droplets freeze on impact (FF = 1); this type of ice is porous, brittle and has a white appearance. When the FF is close to 0, glaze (or clear) ice forms. Glaze ice is dense, hard, and transparent. Between rime and glaze ice two intermediate mixed ice types were tested, too.

Once the ice is accreted on the surface of the samples, the interfacial shear stress between the ice and the surface can be measured.^[50] The results are reported in **Figure 2a–d**, respectively for the rime, mixed/rime, mixed/glaze, and glaze ice conditions. In every chart the value of the reference untreated Ti64 sample is displayed as a solid horizontal line. Samples that exhibit an interfacial shear stress lower than the reference line have reduced ice adhesion strength with respect to the reference and hence show an increased ice release performance.^[7] In all conditions, the DLIP and LIPSS surfaces show an ice adhesion strength lower than the reference, LOTUS 1 and 2 are either slightly below or on the same level than the reference, while ROUGH 1 and 2 and the POROUS surfaces have decreased performances with respect to the reference. The laser-generated structures interact with the impinging droplets and affect the adhesion of the first layer of ice only, since it was observed that ice accreted similarly on all surfaces, meaning that these types of surfaces do not affect the ice accretion process but only the ice adhesion strength.

The comparison of the ice adhesion strengths displayed in **Figure 2a–d** leads to conclude that different atmospheric icing conditions (i.e., FF) have a non-negligible effect on the ice adhesion strength (to facilitate the reader, the four charts were merged in **Figure S2**, Supporting Information). Generally, all samples showed decreased interfacial shear stresses at FF between 0.2 and 0.7, while at FF = 1.0 ice adhesion strength is maximum. This evidence can be explained by the mechanism of ice formation. When the FF = 1.0 (rime ice), the impinging supercooled droplets freeze on impact. Such hit-and-stick mechanism is

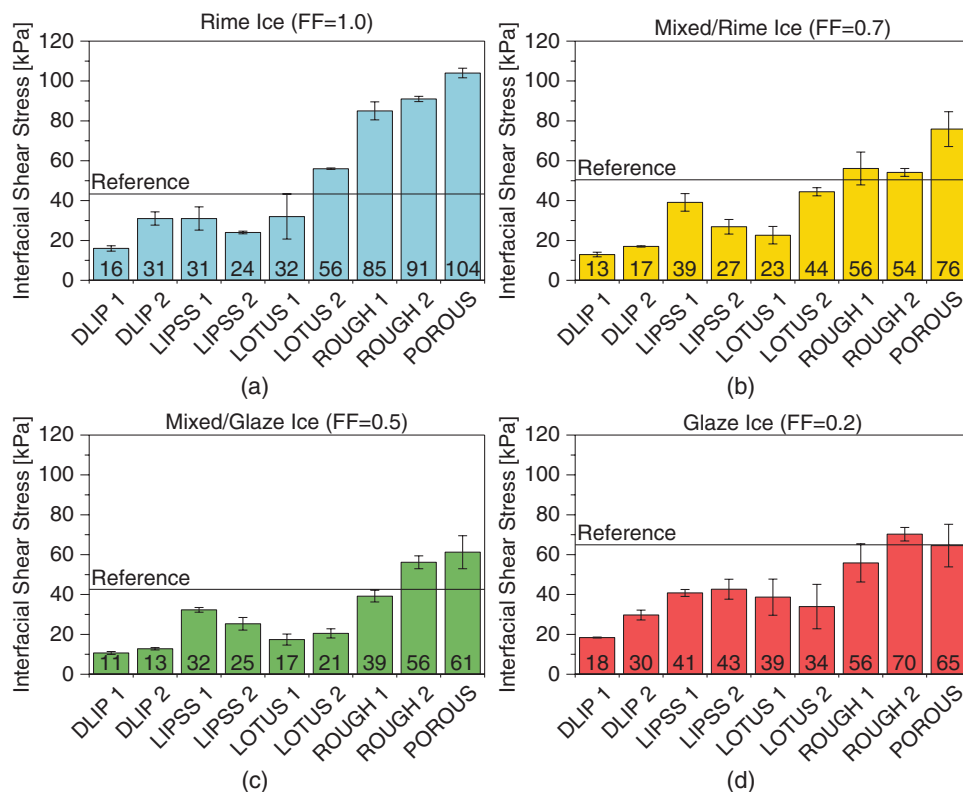


Figure 2. Interfacial shear stress of the laser-treated samples in a) rime ice, b) mixed/rime ice, c) mixed/glaze, and d) glaze ice conditions. The horizontal solid black line represents the interfacial shear stress of the reference Ti64 untreated surface.

dictated by the nucleation rate of the droplets, which increases when the temperature decreases.^[17] Therefore, in this condition the droplet mobility after impact and hence the ability of a surface to repel a supercooled water droplet is strongly limited.

Not only atmospheric conditions but also different superhydrophobic surfaces affect differently the ice adhesion strength. In the rationale behind this observation lies in the different features generated with the various laser methods and fabrication parameters. In the inset of **Figure 3a**, a schematic representation of a laser-generated structure is shown to facilitate the discussion of the results. Λ is the spatial period (i.e., pillar-to-pillar distance) and R_z is the measure of the maximum depth of the structures. For all ice types, ROUGH 1 and ROUGH 2

samples show higher ice adhesion with respect to the reference Ti64. ROUGH 1 and ROUGH 2 are not able to effectively repel water and ice because the spatial period Λ of the structures ($\approx 26 \mu\text{m}$) is comparable to the supercooled droplet size ($\approx 20 \mu\text{m}$) (Figure 3a). At this length scale, the superhydrophobic microstructured surfaces cannot repel micrometric supercooled water droplets that are small enough to fill out the air gaps between the topographic features (Figure 3a). The contact area between ice and surface is larger than on the reference Ti64 surface and hence the mechanical interlocking between ice and surface structures will cause stronger adhesion.^[54]

Ice adhesion on the POROUS surface is also increased for all ice types with respect to the reference Ti64. The laser-generated

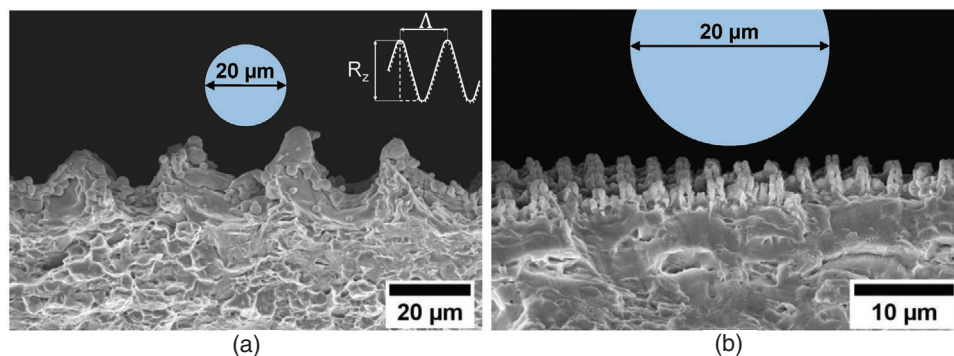


Figure 3. Side view SEM image of the a) ROUGH 2 (1000X) and b) DLIP 1 (2500X) surfaces compared to a water droplet of 20 μm .

micro/nanostructured surface is extremely inhomogeneous (Figure 1i,j), with a Λ of the structures similar or larger than the MVD. Therefore, the air pockets are distributed unevenly on the surface, leaving large areas where the droplets can impinge and freeze on very deep structures, sinking in the asperities and producing a Wenzel wetting state. As consequence, a strong mechanical interlocking occurs upon water freezing.

The spatial period Λ of the samples DLIP 1 and 2 and LIPSS 1 and 2 is at least one order of magnitude lower than MVD (Figure 3b). It is suggested that at this length scale superhydrophobicity of the surfaces is preserved because the structure scale is so small that it is able to repel the micrometric supercooled water droplets. Thus, the Cassie–Baxter wetting state is retained, resulting in lower ice adhesion compared with the reference Ti64 surface.

Insofar can be concluded that two mechanisms may explain the improved performances: i) being in a nonwetting state, the contact area between the accreted ice and the surface is lower than on a flat surface; ii) as it has been proposed in literature,^[55] the air pockets left between the surface and the ice act as stress concentrators. Similar to what happens in bonding technologies,^[56] air pockets can be treated as defects at the surface-ice interface and can trigger interfacial fractures at much smaller surface deformations than on the reference surface, hence allowing debonding the ice at smaller strains. The second mechanism may also explain why the DLIP structures perform better than the LIPSS. The hierarchical surface structures on the DLIP trap a larger volume of air between the micropillars and therefore produce a higher stress concentration at the interface due to the larger dimension of the defects. Since the LIPSS samples use only nanostructures to repel the supercooled water droplets, the amount of air trapped in its valleys is much lower. The lower adhesion strength on DLIP 1 with respect to DLIP 2 can be explained as follows: on both surfaces, the larger air pockets guarantee an effective stress concentration, but on the DLIP 1 the smaller Λ (2.7 instead of 5.4 μm) enables twice as many stress concentration sites and hence reduces the ice adhesion strength.

The LOTUS 1 and LOTUS 2 samples show lower ice adhesion with respect to the reference surface, despite the size of Λ is similar to the MVD. Both surfaces are covered homogeneously with LIPSS (see Figure 1e,f), forming a nanometric roughness superimposed on the micrometric features and producing a hierarchical structure. As a result, the supercooled water droplets can penetrate between the micrometric features but are still repelled by nanostructures and can thus retain the Cassie–Baxter state (detailed SEM images of this structure can be found in Figure S3, Supporting Information).

In summary, a Cassie–Baxter state can be achieved by the combination of low surface free energy and surface roughness. The spatial period of the features defining the roughness must be small enough to support carefully deposited or violently impinging water droplets of different sizes. A Cassie–Baxter behavior is thus not exclusively a surface property, but it depends on more parameters. A transition from a nonwetting Cassie–Baxter state to a wetting Wenzel state^[57] can occur, in which the droplets fill the cavities within the structures. In particular, in the Wenzel state, the increased surface area with respect to a flat surface has a strong negative impact on the ice adhesion strength. The trapped ice acts as an anchor on the substrate, enhancing the mechanical interlocking. In this case, the depth of the laser-generated surface structures is relevant and directly related to the degree of mechanical interlocking between surface and ice.

In order to better understand the effects of spatial period Λ and mechanical interlocking are described in Figure 4a,b). Ice adhesion strength is plotted as function of the spatial period Λ in Figure 4a for those surfaces with spatial period Λ smaller than the MVD. For all icing conditions the lowest ice adhesion strength was measured on the DLIP 1 surface. In Figure 4b, the ice adhesion strength is plotted as function of the peak-to-peak roughness R_z for those surfaces with $\Lambda > \text{MVD}$. Since ice adhesion on these surfaces is markedly higher, R_z (representing the depth of the structures) seems a better indicator than the spatial period Λ . The experimental data follow a clear trend: deeper structures (i.e., higher R_z) cause higher ice

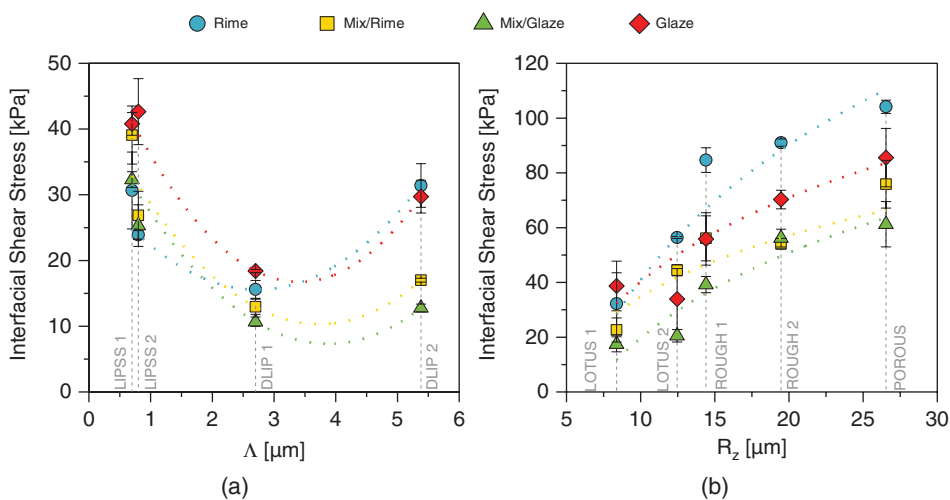


Figure 4. Interfacial shear stress of the laser-treated samples with respect to a) Λ and b) R_z in rime (light blue), mixed/rime (yellow), mixed/glaze (green), and glaze ice (red) conditions. In (a) appear the LIPSS 1, LIPSS 2, DLIP 1, and DLIP 2 surfaces only, while in (b) the LOTUS 1, LOTUS 2, ROUGH 1, ROUGH 2, and POROUS surfaces. The dotted splines are meant to guide the eye of the reader only.

adhesion and is due to stronger mechanical interlocking. Such trend was already observed and discussed in literature.^[58,59] Even though LOTUS 1 and 2 perform better than the reference and retain a Cassie–Baxter State due to their surface nanostructures, the ice fills the microstructures and causes mechanical interlocking.

Since the mechanical interlocking effect can be also associated to the total contact area between the ice and the surface, the interfacial shear stress was plotted as function of the product between the spatial period and the surface roughness ($\Lambda \cdot R_z$) (Figure 5).

For all icing conditions two dominant factors affect the ice adhesion strength: the interfacial shear stress increases for smaller $\Lambda \cdot R_z$ due to the smaller dimension of the air pockets and hence the lower stress concentration induced at the interface between ice and surface. The shear stress is minimum in correspondence of the DLIP 1 surface, where the air pockets are large enough to induce an effective stress concentration, but still Λ is small enough to avoid penetration of droplets into the air pockets. Finally, for larger $\Lambda \cdot R_z$ the interfacial shear stress increases due to the mechanical interlocking between ice and surface caused by the penetration of the droplets between the structures. This behavior holds for all four icing cases investigated. In conclusion, design rules can be defined in order to

produce surfaces with icephobic properties. The laser-generated surface structures, providing superhydrophobic properties, should have a spatial period Λ of few μm and a second scale roughness in the nm range (i.e., LIPSS) in order to tackle/reduce ice adhesion. In particular, a Λ of an order of magnitude smaller than the MVD is preferred, since the surface structures are small enough to repel the impinging droplets and the air pockets left underneath are large enough to induce an effective stress concentration at the interface with the accreted ice. It is expected that surfaces produced following such design rules will behave more effectively in mixed/rime, mixed/glaze, and glaze ice, due to higher droplet mobility in these conditions before freezing.

2.3. Wetting States of Impinging Droplets on Superhydrophobic Surfaces

Ice adhesion strength on the DLIP 1 surface was the lowest. The improved performances of such micro/nanostructured surfaces could be explained with the retention of the Cassie–Baxter state in in-flight icing conditions. To support this hypothesis, investigations of the impact of μm -sized droplets were performed using a high-speed camera (PHOTRON

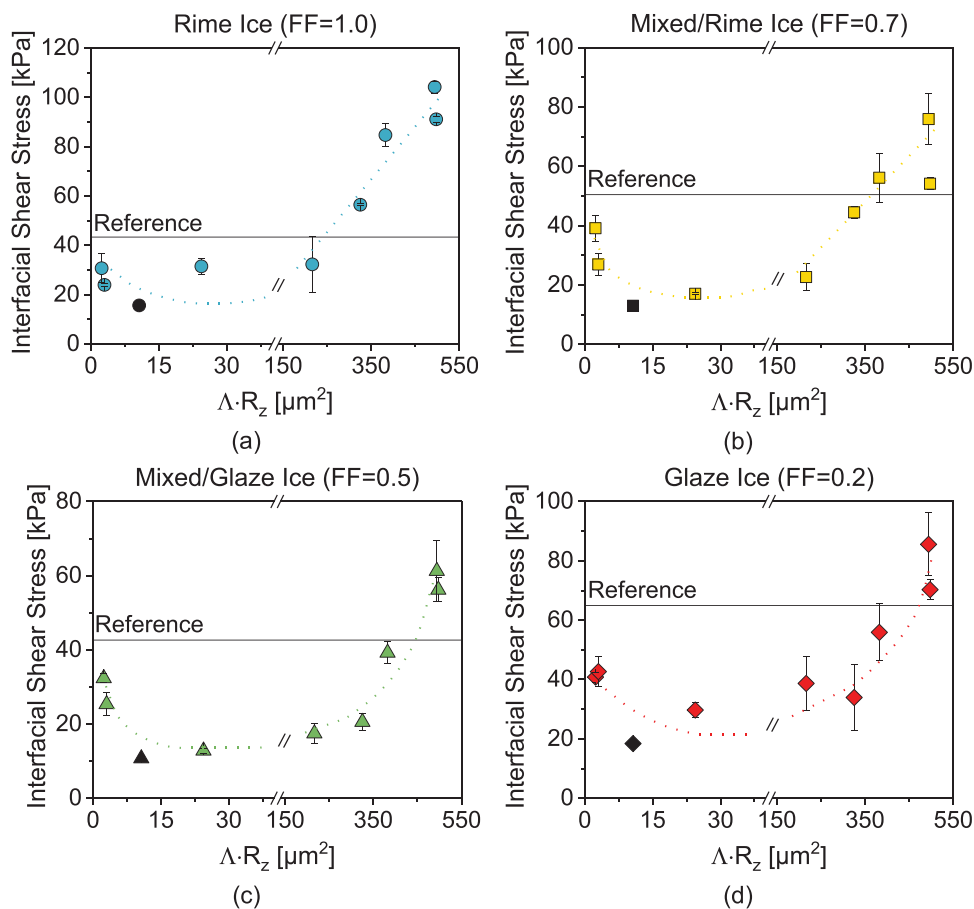


Figure 5. Interfacial shear stress of the laser-treated samples with respect to the arbitrary parameter $\Lambda \cdot R_z$ in a) rime, b) mixed/rime, c) mixed/glaze, and d) glaze ice conditions. The horizontal solid black lines represent the interfacial shear stress on the reference Ti64, while the dashed spline is meant only to guide the eye of the reader. The symbols associated with the DLIP 1 are filled in black (error bars are smaller than the symbol).

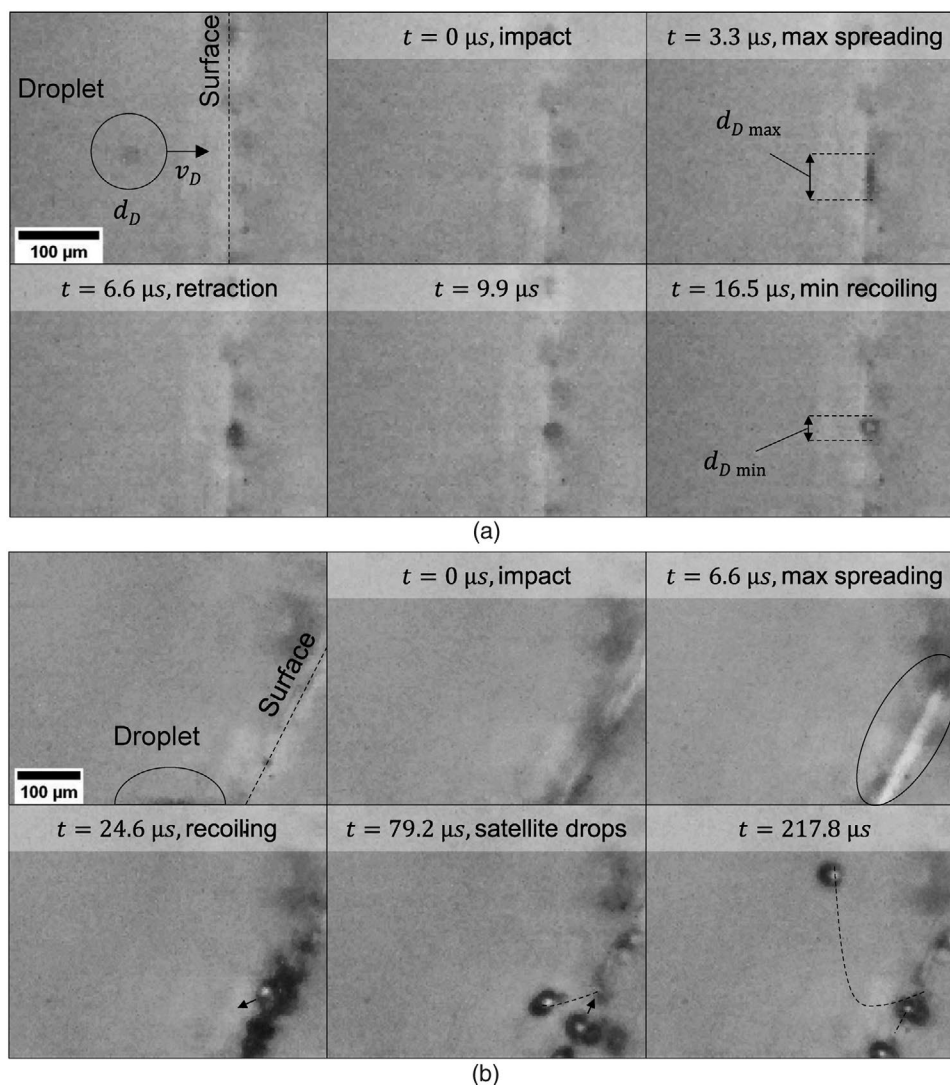


Figure 6. Water droplet impacting on the DLIP 1 surface at room temperature. a) TAS = 50 m s^{-1} , AoA = 90° , frame rate = 300 000 fps, shutter speed = $0.16 \mu\text{s}$. The droplet speed and diameter are respectively $v_D = 32 \text{ m s}^{-1}$ and $d_D = 20 \mu\text{m}$. b) TAS = 80 m s^{-1} , AoA = 60° , frame rate = 300 000 fps, shutter speed = $0.35 \mu\text{s}$. The droplet speed and diameter are respectively $v_D = 55 \text{ m s}^{-1}$ and $d_D = 80\text{--}100 \mu\text{m}$.

Fastcam SA-Z Type 2100K). The tests were carried out at room temperature only.

Figure 6a shows the frames taken from a high-speed video of a droplet impacting on the DLIP 1 surface. The TAS was set to 50 m s^{-1} . The droplet speed v_D , calculated from the two frames before the impact, is $\approx 32 \text{ m s}^{-1}$. The difference between the TAS and the v_D is due to the aerodynamic braking of the droplet and the airstream caused by the sample, having 90° angle of attack (AoA) with respect to the airflow. The droplet size d_D was calculated in the last frame before the impact and was $\approx 20 \mu\text{m}$ (resolution $3.125 \mu\text{m}$ per pixel). After the impact the droplet spread on the surface reaching the maximum spreading diameter $d_{D \max}$. Subsequently, the droplet recoiled to a more spherical shape, typical of a strongly hydrophobic or superhydrophobic surface, until reaching the minimum recoiling diameter $d_{D \min}$.

Figure 6b shows high-speed images from a different test. This test is not representative of the ice adhesion test

configuration, since the AoA is 60° and the droplet dimension is much larger than the MVD (order of $d_D = 80\text{--}100 \mu\text{m}$). The TAS was set to 80 m s^{-1} , which resulted in a droplet speed before impact v_D of 55 m s^{-1} . As a consequence of the impact, satellite droplets were generated. Such droplets regained a spherical shape and did not stick to the surface. One droplet bounced off from the impact area, left the boundary layer and was transported away by the airstream. A second one, rolled on the surface until resting in a spherical shape typical of a non-wetting Cassie–Baxter state.

In literature, different models were proposed to describe the impact dynamics of water drops on superhydrophobic surfaces.^[60–62] Most models agree that the wetting state resulting after the impact depends on the balance between nonwetting and wetting pressures. The pressures playing a role into this balance are: the dynamic or Bernoulli pressure ($P_D = 1/2\rho v^2$, where ρ and v are respectively the droplet density and velocity),

the capillary pressure ($P_C = -2\sqrt{2} \gamma_{LA} \cos\theta_A / \Lambda$, where γ_{LA} is the surface energy of the water at water-vapor interface, θ_A is the static contact angle of the droplet, and Λ is the spatial period of the structure), and the water hammer pressure ($P_{WH} \approx 0.2\rho cv$, where c is the speed of sound in water) generated by the shock wave originating at impact.^[61] A nonwetting state occurs when the sum of the water hammer pressure and the dynamic pressure (both wetting pressures) do not exceed the capillary pressure (nonwetting pressure), i.e., when $P_C > P_{WH} + P_D$, Figure S4a in the Supporting Information. Otherwise, either partial ($P_{WH} > P_C > P_D$, Figure S4b, Supporting Information) or total wetting ($P_{WH} > P_D > P_C$, Figure S4c, Supporting Information) can occur. Regardless of the surface or test condition, all impacts investigated in this work would produce a total wetting state (Wenzel state). Experimental evidences of microimpacts, however, show a different behavior. For the case shown in Figure 6a, the calculated pressure values for P_{WH} , P_D , and P_C are respectively ≈ 10.78 , 0.65 , and 0.07 MPa, which would lead to a total wetting state ($P_{WH} > P_D > P_C$). However, in case of a total wetting, the droplet would then remain pinned into its position without experiencing the experimentally observed recoiling. Partial wetting could originate from the impact, since the high water hammer pressure should cause the collapsing of at least some air pockets underneath the impact area. Even in this case, though, the droplet could still move onto the surface on top of several noncollapsed air pockets. The calculated pressures P_{WH} , P_D , and P_C for the case shown in Figure 6b are ≈ 16.46 , 1.51 , and 0.07 MPa, respectively. Again, a total wetting state ($P_{WH} > P_D > P_C$) is expected.

Using the model proposed by Deng et al.,^[61] a nonwetting state is predicted only for structures with a spatial period Λ of 75 and 125 nm considering impact speeds correspondingly of 80 and 50 m s⁻¹ (with constant $\rho = 1000$ kg m⁻³, $c = 1500$ m s⁻¹, $\gamma_{LA} = 0.72$ N m⁻¹, and $\theta_A = 160^\circ$). Vice versa, considering a spatial period Λ of 2.7 μ m (i.e., DLIP 1), a nonwetting state could be achieved only for impact speeds of ≈ 2 ms. Thus, the models available in literature, which are able to describe the wetting state originating by the impact of raindrop ($\approx 1\text{--}3$ mm) on a superhydrophobic surface, so far fail to describe what has been observed in this research. Hence, new models should be proposed and validated that can explain the experimental data on high-speed microscopic droplets presented in this work. The current models should be refined and additional parameters like droplet and surface temperature and droplet viscosity have to be considered. In the new/refined models droplets with diameters in the order of tens of micrometer have to be considered instead of millimeter-sized droplets—even if according to the commonly used scaling this may not be relevant. Otherwise, the scaling employed does not take into account size effects that play a role when analyzing icephobicity of threatened surfaces. In particular, when droplets in the micrometer scale and smaller are considered electrostatic and van der Waals interactions or capillary effects may become relevant and of similar magnitude to the momentum of the droplets and inertial forces.

3. Conclusions

Superhydrophobic properties were achieved on Ti64 substrates with three different laser processing methods, i.e., DLW, DLIP,

and LIPSS, with pulse durations in the range from hundreds of nanoseconds down to hundreds of femtoseconds, combined with a chemical functionalization. The adhesion strength of the ice on surface structures produced employing these methods was investigated in icing wind tunnel tests under four representative in-flight icing conditions. It was found that icephobicity was dependent on the spatial period Λ of the structures and it had to be at least one order of magnitude smaller than the MVD. In this way, Cassie–Baxter nonwetting state can be retained and the processed surfaces can exhibit icephobic properties. A lower ice-surface contact area and a stress concentration induced by the air pockets can explain the improved icephobic performance on such surfaces. Once a transition from the Cassie–Baxter state to the Wenzel state occurs, the depth of the structures has a direct influence on the mechanical interlocking between ice and surface. There are two opposite factors affecting the surface response, i.e., stress concentrations and lower surface contact area versus mechanical interlocking. The ice adhesion behavior of hierarchical micro/nanostructures produced with the DLIP process was the lowest achieved with the investigated laser processed surfaces. Additionally, the icing conditions (i.e., the freezing fraction) had an impact on the effectiveness of the considered superhydrophobic surfaces. Especially, the droplets froze faster at higher freezing fractions and thus decreased the ability of the processed surfaces to repel them effectively while they were still liquid. On the other hand, at low freezing fractions the liquid water could fill up the surface structures to some extent before freezing and thus to increase the ice-surface mechanical interlocking. In the less severe intermediate conditions, the surfaces were able to repel more effectively the supercooled water droplets.

Further research is required to understand the influence of different icing parameters on ice adhesion and to assess the compatibility and robustness of such surfaces in operational environment (i.e., rain and sand erosion, UV resistance, interaction with other fluids, such as hydraulic and anti-icing). Additionally, the models describing the impact dynamics and wetting states of impinging droplets on structured surfaces were found not applicable to the present study. Most likely, this was due to the limited number of parameters considered by the models—among which the size of droplets and/or the size of surface structures seems to play a critical role. Taking into account more parameters could expand the validity of the existing models.

4. Experimental Section

Materials: Substrates of Ti6Al4V (Ti64) (VSMPO, Verkhnyaya Salda, Russia) with a thickness of 1 mm were used for all experiments in this work, cut in the size of 125 mm by 13 mm in order to fit the ice adhesion test setup. The material was chosen due to its widespread use in the aeronautic industry. Prior to laser processing, the substrates were cleaned from contaminations by rinsing with isopropanol and drying with compressed air. After the laser processing, the surfaces were functionalized to reduce their surface free energy and generate superhydrophobic properties via the commercial product MecaSurf (Surfactis Technologies, Angers, France). MecaSurf is a chemically active perfluoropolyether compound dissolved in a fluorinated solvent and it is applied on the laser-treated samples by dip coating for 5 min and then drying in air.

DLW and LIPSS: Two different laser sources were used to manufacture the surface structures:

- 1) A linearly polarized femtosecond (fs) laser (Satsuma, Amplitude Systemes, France) with 310 fs pulses at a wavelength of 1032 nm and a maximum average power of 5 W.
- 2) A randomly polarized nanosecond (ns) laser (redENERGY G4 50W HS-S, SPI Laser, UK) with 15 ns pulses at wavelength of 1064 nm and a maximum average power of 50 W.

The laser system is shown in Figure S5 in the Supporting Information. The optical path included a half wave plate to vary the polarization direction of the fs-laser beam. A beam expander and a 100 mm telecentric focusing lens were used to achieve a beam spot size of $\approx 30 \mu\text{m}$ diameter (d) in the focal plane with a Gaussian energy distribution, both for ns-DLW, fs-DLW, and fs-LIPSS processing methods. The substrates were positioned in the focal plane of the beam delivery system and a 3D scan head (RhoThor RTA, Newson, Belgium) was used to steer the beam over the surfaces in raster patterns. The DLW process was performed with pulse repetition rates from 100 to 500 kHz with fluence from $\phi = 0.07$ to 3.11 J cm^{-2} . The other laser processing parameters considered in this research were the hatch distance (h_d) between the scan lines, the scanning speed (v_s), the number of scans, and the scanning strategy (line-like or cross-like). The linear (O_l) and vertical (O_v) pulse-to-pulse overlaps were calculated using $O_l = 1 - (v_s/f)/d$ and $O_v = 1 - h_d/d$.

DLIP: The experimental two-beam-DLIP setup includes an IR picosecond (ps) laser (solid-state Q-switched Innoslab Nd:YVO4, Edgewave, Germany) emitting 10 ps pulses at the wavelength of 1064 nm and a repetition rate of 10 kHz, with a TEM00 beam intensity distribution and $M^2 < 1.1$. For the interference patterning setup, a compact optical head (developed at Fraunhofer Institut für Werkstoff- und Strahltechnik (IWS)) allowed the splitting of the main laser beam into two sub-beams, which are overlapped on the sample surface with a determined angle θ (see Figure S6, Supporting Information). The angle θ can be automatically varied and controlled in the optical head, which together with the laser wavelength (λ) determines the spatial period (Λ) of the micropattern ($\Lambda = \lambda/(2 \sin \theta)$). Additional information about the developed optical DLIP heads is already published in ref. [63].

In the experiments spatial periods Λ of 2.7 and $5.4 \mu\text{m}$ were used, which corresponded to angles θ of 11.8° and 5.9° , respectively. The diameter of the area, on which the interference pattern is produced (section of the interference volume), was set to $285 \mu\text{m}$. To extend the micropatterned area, the sample was moved in the lateral directions (XY), according to the processing strategy reported in ref. [47]. The overlap of pulses was performed in the y -direction (scan direction) with a pulse-to-pulse overlap of 99%. In the x -direction, the pulses were separated by a hatch distance of $275.6 \mu\text{m}$ in order to ensure a homogeneous coverage of the processed area. For the fabrication of pillar-like microstructures, the samples were first irradiated to fabricate line-like structures and after that were rotated in the x - y plane and reirradiated. The fluence was constant during both irradiations ($\phi = 0.57 \text{ J cm}^{-2}$).

All laser experiments (DLW and DLIP) were carried out under normal ambient-pressure conditions.

Surface Characterization: The AURIGA Crossbeam 550 Scanning Electron Microscopy (ZEISS, Germany) was used to characterize the surface morphology of the laser-treated samples. The measurements of the surface roughness were performed with the DektakXT Stylus Profiler from Brüker, repeating every measurement point three times for statistical purposes. The wettability of the samples was evaluated by measuring the static CA and the roll-off angle (RoA) using a video-based optical contact angle-measuring device and the sessile drop technique in atmospheric environment (environmental temperature of 20°C). The measurements were performed six times using $10 \mu\text{L}$ droplets of deionized water with the instrument Drop Shape Analyzer DSA25 by Krüss GmbH (Hamburg, Germany) and the software ADVANCE.

Table 2. Icing conditions used for the ice adhesion tests. TAT: total air temperature; TAS: true air speed; MVD: median volume diameter; FF: freezing fraction.

Ice type	TAT [$^\circ\text{C}$]	TAS [m s^{-3}]	LWC [g m^{-3}]	MVD [μm]	Approximate FF
Rime	-20	50	0.3	20	1.0
Mixed/rime	-20	50	0.8	20	0.7
Mixed/glaze	-5	50	0.3	20	0.5
Glaze	-5	80	1.0	20	0.2

Icing Wind Tunnel: The icephobic properties of the laser-treated surfaces were tested in the iCORE (icing and COntamination REsearch) facility.^[50] The iCORE is a lab-sized icing wind tunnel in a Göttingen configuration (i.e., circular closed loop wind tunnel) located in Airbus Central R&T. The iCORE can simulate atmospheric in-flight icing conditions, with an MVD of the supercooled water droplets of $\approx 20 \mu\text{m}$, since this value corresponds to the typical drop size in clouds and in accordance to the Icing Design Envelopes collected in Appendix C^[51] specifications from the Federal Aviation Administration. The MVD is defined as the midpoint droplet size (median), where half of the water volume in the cloud is in droplets smaller, and half of the volume is in droplets larger than the median.^[51]

A vibrating cantilever test rig developed by Strobl et al.^[64] was used to evaluate the adhesion strength of the ice on different laser-treated samples and compared to the reference untreated Ti64 surface; such test rig allows the measurement of the interfacial shear stress for the ice layer to debond from the substrate that is the ice adhesion strength. During a test, a sample in the shape of a cantilever of $125 \times 13 \text{ mm}^2$ is fixed from one end on an electromagnetic shaker. Atmospheric ice is accreted on the tested surface and then removed via mechanical vibration.^[64,65] The shear stress at the interface between the accreted ice layer and the cantilever is measured by a strain gauge and used to characterize the ice interfacial shear strength. For clarity, a high speed video of a typical ice adhesion test run is available in the Supporting Information.

The four different icing conditions used are listed in Table 2. The approximate FF calculation reported in Table 2 is based on work carried out at Cranfield University.^[66] High-speed videos were recorded to investigate the behavior of micrometer sized droplets impacting on a laser-treated surface. The camera used was a PHOTRON Fastcam SA-Z Type 2100K, mounting a Long Distance Microscope Questar QM-100, with the following settings: 300 000 frames s^{-1} , resolution of 256×128 -pixel, and shutter speed time of 0.16 and $0.35 \mu\text{s}$. Both the light source and the camera were placed at roughly 30 cm from the area of interest on the sample in a backlight configuration, with a resolution of $3.125 \mu\text{m}$ per pixel. Both the lighting and the camera were set at a shallow angle relative to the sample test surface to maximize the light acquisition of the camera and to avoid shadows produced by droplets outside the focal plane to overlap with the area of interest (see Figure S7, Supporting Information). In order to further maximize the light intake, the input light was focused on a point which intersected both the test sample and the focal plane of the camera. The data recorded were processed using the Photron Fastcam Viewer (PFV4) software after previous calibration of the camera.

Supporting Information

Supporting Information is available from the Wiley Online Library or from the author.

Acknowledgements

The authors would like to thank Alexandre Laroche for his relevant work on this topic, Norbert Karpen and Alexandre Cuco for helping in the data

analysis, and Max Kolb for the SEM pictures. V.V. and S.T. would like to thank Giovanni Pulci and Francesco Marra for the stimulating discussions. This research was carried out in the framework of the LASER4FUN project (www.laser4fun.eu), which has received funding from the European Union's Horizon 2020 research and innovation programme under the Marie Skłodowska-Curie Grant Agreement No. 675063.

Conflict of Interest

The authors declare no conflict of interest.

Keywords

icephobic, icing, laser processing, micro/nanopatterning, superhydrophobic

Received: December 10, 2019

Revised: January 17, 2020

Published online:

- [1] M. B. Bragg, A. P. Broeren, L. A. Blumenthal, *Prog. Aerosp. Sci.* **2005**, *41*, 323.
- [2] J. M. Diebold, A. P. Broeren, M. B. Bragg, in *5th AIAA Atmospheric and Space Environments Conference*, San Diego, CA **2013**, pp. 1–20.
- [3] M. J. Kreder, J. Alvarenga, P. Kim, J. Aizenberg, *Nat. Rev. Mater.* **2016**, *1*, 15003.
- [4] A. Work, Y. Lian, *Prog. Aerosp. Sci.* **2018**, *98*, 1.
- [5] L. Makkonen, *J. Adhes. Sci. Technol.* **2012**, *26*, 413.
- [6] A. J. Meuler, J. D. Smith, K. K. Varanasi, J. M. Mabry, G. H. McKinley, R. E. Cohen, *ACS Appl. Mater. Interfaces* **2010**, *2*, 3100.
- [7] K. Golovin, S. P. R. Kobaku, D. H. Lee, E. T. DiLoreto, J. M. Mabry, A. Tuteja, *Sci. Adv.* **2016**, *2*, 1.
- [8] B. R. Kim, *Environ. Eng. Res.* **2011**, *16*, 1.
- [9] W. Barthlott, C. Neinhuis, *Planta* **1997**, *202*, 1.
- [10] K. Koch, B. Bhushan, W. Barthlott, *Prog. Mater. Sci.* **2009**, *54*, 137.
- [11] L. Gao, T. J. McCarthy, *Langmuir* **2006**, *22*, 2966.
- [12] A. B. D. Cassie, S. Baxter, *Trans. Faraday Soc.* **1944**, *40*, 546.
- [13] L. Mishchenko, B. Hatton, V. Bahadur, J. A. Taylor, T. Krupenkin, J. Aizenberg, *ACS Nano* **2010**, *4*, 7699.
- [14] C. Antonini, M. Innocenti, T. Horn, M. Marengo, A. Amirfazli, *Cold Reg. Sci. Technol.* **2011**, *67*, 58.
- [15] T. M. Schutzius, S. Jung, T. Maitra, P. Eberle, C. Antonini, C. Stamatopoulos, D. Poulidakos, *Langmuir* **2015**, *31*, 4807.
- [16] J. C. Bird, R. Dhiman, H. M. Kwon, K. K. Varanasi, *Nature* **2013**, *503*, 385.
- [17] A. Alizade, M. Yamada, R. Li, W. Shang, S. Otta, S. Zhong, L. Ge, A. Dhinojwala, K. R. Conway, V. Bahadur, A. J. Vinciguerra, B. Stephens, M. L. Blohm, *Langmuir* **2012**, *28*, 3180.
- [18] L. Wang, M. Wen, M. Zhang, L. Jiang, Y. Zheng, *J. Mater. Chem. A* **2014**, *2*, 3312.
- [19] S. Milles, M. Soldera, B. Voisiat, A. F. Lasagni, *Sci. Rep.* **2019**, *9*.
- [20] L. B. Boinovich, A. M. Emelyanenko, *Mendeleev Commun.* **2013**, *23*, 3.
- [21] Y. Shen, X. Wu, J. Tao, C. Zhu, Y. Lai, Z. Chen, *Prog. Mater. Sci.* **2019**, *103*, 509.
- [22] D. De Pauw, A. Dolatabadi, *J. Aircr.* **2017**, *54*, 490.
- [23] Y. Shen, G. Wang, J. Tao, C. Zhu, S. Liu, M. Jin, *Adv. Mater. Interfaces* **2017**, *1700836*, 1.
- [24] Y. Y. Yan, N. Gao, W. Barthlott, *Adv. Colloid Interface Sci.* **2011**, *169*, 80.
- [25] W. S. Y. Wong, Z. H. Stachurski, D. R. Nisbet, A. Tricoli, *ACS Appl. Mater. Interfaces* **2016**, *8*, 13615.
- [26] L. Wermuth, M. Kolb, T. Mertens, T. Strobl, D. Raps, *Prog. Org. Coat.* **2015**, *87*, 242.
- [27] J. T. Cardoso, A. Garcia-Girón, J. M. Romano, D. Huerta-Murillo, R. Jagdheesh, M. Walker, S. S. Dimov, J. L. Ocaña, *RSC Adv.* **2017**, *7*, 39617.
- [28] A. Garcia-Girón, J.-M. Romano, Y. Liang, B. Dashtbozorg, H. Dong, P. Penchev, S. S. Dimov, *Appl. Surf. Sci.* **2018**, *439*, 516.
- [29] J.-M. Romano, M. Gulcur, A. Garcia-Giron, E. Martinez-Solanas, B. R. Whiteside, S. S. Dimov, *Appl. Surf. Sci.* **2019**, *476*, 850.
- [30] F. Chen, D. Zhang, Q. Yang, J. Yong, G. Du, J. Si, F. Yun, X. Hou, *ACS Appl. Mater. Interfaces* **2013**, *5*, 6777.
- [31] V. Lang, T. Roch, A. F. Lasagni, *Adv. Eng. Mater.* **2016**, *18*, 1342.
- [32] V. Lang, T. Roch, A. F. Lasagni, in *Proc. SPIE* **2016**, *9736*, 97360Z-1.
- [33] F. Jansen, A. Budnicki, D. Sutter, *Laser Tech. J.* **2018**, *15*, 46.
- [34] M. Soldera, Q. Wang, F. Soldera, V. Lang, A. Abate, A. F. Lasagni, *Adv. Eng. Mater.* **2020**, *1901217*, 1.
- [35] B. Wu, M. Zhou, J. Li, X. Ye, G. Li, L. Cai, *Appl. Surf. Sci.* **2009**, *256*, 61.
- [36] R. Jagdheesh, J. J. García-Ballesteros, J. L. Ocaña, *Appl. Surf. Sci.* **2016**, *374*, 2.
- [37] M. V. Rukosuyev, J. Lee, S. J. Cho, G. Lim, M. B. G. Jun, *Appl. Surf. Sci.* **2014**, *313*, 411.
- [38] D. Huerta-Murillo, A. I. Aguilar-Morales, S. Alamri, J. T. Cardoso, R. Jagdheesh, A. F. Lasagni, J. L. Ocaña, *Opt. Lasers Eng.* **2017**, *98*, 134.
- [39] G. Römer, M. N. W. Del Cerro, D. A. Groenendijk, A. J. Huis, R. C. J. Sipkema, *29th Int. Congr. Appl. Lasers Electro-Optics, ICALEO 2009*, 2009, 30.
- [40] J. Long, P. Fan, D. Gong, D. Jiang, H. Zhang, L. Li, M. Zhong, *ACS Appl. Mater. Interfaces* **2015**, *7*, 9858.
- [41] Y. Liu, X. Li, Y. Yan, Z. Han, L. Ren, *Surf. Coat. Technol.* **2017**, *331*, 7.
- [42] V. Vercillo, J. T. Cardoso, D. Huerta-Murillo, S. Tonnicchia, A. Laroche, J. A. Mayén Guillén, J. L. Ocaña, A. F. Lasagni, E. Bonaccorso, *Mater. Lett. X* **2019**, *3*, 1.
- [43] D. Huerta-Murillo, A. García-Girón, J. M. Romano, J. T. Cardoso, F. Cordovilla, M. Walker, S. S. Dimov, J. L. Ocaña, *Appl. Surf. Sci.* **2019**, *463*, 838.
- [44] G. R. B. E. Römer, J. Z. P. Skolski, J. V. Obona, A. J. Huis In't Veld, *Phys. Procedia* **2014**, *56*, 1325.
- [45] J.-M. Romano, A. Garcia-Giron, P. Penchev, S. Dimov, *Appl. Surf. Sci.* **2018**, *440*, 162.
- [46] S. Alamri, M. El-khoury, A. I. Aguilar-Morales, S. Storm, T. Kunze, A. F. Lasagni, *Sci. Rep.* **2019**, *9*, 1.
- [47] A. I. Aguilar-Morales, S. Alamri, A. F. Lasagni, *J. Mater. Process. Technol.* **2018**, *252*, 313.
- [48] S. Alamri, A. F. Lasagni, *Opt. Express* **2017**, *25*, 9603.
- [49] J. L. Ocaña, R. Jagdheesh, J. J. García-Ballesteros, *Adv. Opt. Technol.* **2016**, *5*, 87.
- [50] T. Hauk, T. Strobl, D. Raps, in *25th Eur. Conf. Liq. Atomization Spray Syst. (ILASS)*, Chania, Crete **2013**, p. 8.
- [51] R. K. Jeck, *Fed. Aviation Adm.* **2002**, *55*.
- [52] L. Makkonen, *J. Clim. Appl. Meteorol.* **1984**, *23*, 929.
- [53] L. Makkonen, *Atmos. Res.* **1998**, *46*, 131.
- [54] J. Chen, J. Liu, M. He, K. Li, D. Cui, Q. Zhang, X. Zeng, Y. Zhang, J. Wang, Y. Song, *Funct. Ecol.* **2012**, *101*, 111603-1.
- [55] M. Nosonovsky, V. Hejazi, *ACS Nano* **2012**, *6*, 8488.
- [56] A. V. Pocius, *Adhesion and Adhesives Technology: An Introduction*, 3rd ed., Hanser Publishers, Munich, Germany **2012**.
- [57] R. N. Wenzel, *J. Phys. Colloid Chem.* **1949**, *53*, 1466.
- [58] M. F. Hassan, H. P. Lee, S. P. Lim, *Meas. Sci. Technol.* **2010**, *21*, 075701.
- [59] M. Zou, S. Beckford, R. Wei, C. Ellis, G. Hatton, M. A. Miller, *Appl. Surf. Sci.* **2011**, *257*, 3786.

- [60] D. Bartolo, F. Bouamrine, É. Verneuil, A. Buguin, P. Silberzan, S. Moulinet, *Europhys. Lett.* **2006**, *74*, 299.
- [61] T. Deng, K. K. Varanasi, M. Hsu, N. Bhate, C. Keimel, J. Stein, M. Blohm, *Appl. Phys. Lett.* **2009**, *94*, 24.
- [62] S. Dash, M. T. Alt, S. V. Garimella, *Langmuir* **2012**, *28*, 9606.
- [63] M. Bieda, M. Siebold, A. Fabián, *Appl. Surf. Sci.* **2016**, *387*, 175.
- [64] T. Strobl, D. Raps, M. Hornung, *World Acad. Sci. Eng. Technol.* **2012**, *68*, 1673.
- [65] D. S. Thompson, D. Meng, A. Afshar, R. Bassou, J. Zong, E. Bonaccorso, A. Laroche, V. Vercillo, in *2018 Atmospheric and Space Environments Conference*, AIAA, Atlanta, Georgia **2018**, pp. 1–19.
- [66] M. L. Pervier, *Mechanics of Ice Detachment Applied to Turbomachinery*, Cranfield University, Cranfield, UK **2012**.